



Exploring Lithium Storage Mechanism and Cycling Stability of $\text{Bi}_2\text{Mo}_3\text{O}_{12}$ Binary Metal Oxide Anode Composited with Ti_3C_2 MXene

Kai Tian,^[a, b] Hui Lu,^[a, b] Liangmin Bu,^[a, b] Xue Huang,^[a, b] Chao-Lung Chiang,^[c] Shiqi Yang,^[a, b] Yue Zhao,^[a, b] Yan-Gu Lin,*^[c] Jianqing Zhao,^{*[a, b]} and Lijun Gao^{*[a, b]}

Metal oxides are widely evaluated as high-capacity anode candidates for practical lithium ion battery applications, owing to their attractive volumetric and gravimetric capacities compared with the traditional graphite anode. Synergistic effects on improving electrochemical performance of binary metal oxide anodes have been increasingly reported *via* different working mechanisms for lithium storage instead of simple combination of two single components. Herein, we report on exploring lithium storage mechanism in $\text{Bi}_2\text{Mo}_3\text{O}_{12}$ binary metal oxide for the first time as an anode material. *In-situ* synchrotron X-ray diffraction measurements are performed on this exotic material to elucidate lithium storage behaviors, coupled with voltage-resolved cyclic voltammetry and *ex-situ* X-ray photoelectron spectroscopy analyses. The $\text{Bi}_2\text{Mo}_3\text{O}_{12}$ anode undergoes an irreversible initial conversion reaction, resulting in metallic Bi

and Li_2MoO_4 components through electrochemical lithiation. During successive cycling, these two components reversibly uptake and release Li ions through alloying/de-alloying and intercalation/de-intercalation reactions, by forming corresponding Li_2Bi alloy and excessively-lithiated $\text{Li}_{2+x}\text{MoO}_4$ derivative, respectively. Cycling stability of the $\text{Bi}_2\text{Mo}_3\text{O}_{12}$ anode material is considerably enhanced by *in-situ* composition with Ti_3C_2 -based MXene nanosheets. The $\text{Bi}_2\text{Mo}_3\text{O}_{12}@\text{Ti}_3\text{C}_2$ composite anode material can deliver an initial charge capacity of approximately 846 mAh g^{-1} at 50 mA g^{-1} and retain at 227 mAh g^{-1} upon prolonged 1000 cycles at 2.5 A g^{-1} high charge/discharge current density. This work offers some insights into lithium storage mechanism and composite nanostructure design in Bi–Mo–O binary metal oxide anode towards enhanced electrochemical performance.

1. Introduction

Lithium ion batteries have been widely applied in portable electronic devices, pure/hybrid electric vehicles and stationary energy storage in smart grids, owing to high energy density and long service life.^[1–4] The rapid development of electric transportation and large-scale energy storage systems demands improved performance of current Li-ion batteries, which is essentially determined by the electrochemical properties of electrode materials from both cathode and anode sides. Hence, a great deal of academic and industrial efforts has been devoted to develop electrode material alternatives with increased gravimetric/volumetric capacities, desired working

voltages, outstanding cycling stabilities and rate capabilities.^[5–10]

Owing to the low lithium storage capacity of conventional graphite anode material (maximum 372 mAh g^{-1}), it is necessary to seek high-capacity anode alternatives for next-generation Li-ion batteries.^[11] Among various potential candidates, transition metal oxides have been considered promising, since they can deliver high lithium storage capacities more than twice that of graphite anode, along with chemical stability conditions during material synthesis and storage.^[12–19] For example, Mo-based layered oxides, such as MoO_2 and MoO_3 , have been widely reported as anode alternatives for high-energy Li-ion batteries, because of their high theoretical capacities of 838 and 1117 mAh g^{-1} , respectively.^[17–22] However, due to complex lithium storage mechanisms involving surface adsorption/desorption, interfacial intercalation/de-intercalation and conversion reaction,^[23] pristine Mo-based anode materials often show poor cycling stabilities and rate capabilities, especially under cycling at low voltages ($< 1.0 \text{ V vs. Li}^+/\text{Li}$). Another example is the bismuth trioxide (Bi_2O_3), an attractive anode candidate with unique volumetric density and impressive volumetric capacity (3600 mAh cm^{-3}).^[24–27] An irreversible conversion reaction of original Bi_2O_3 anode material takes place during the initial lithiation process, resulting in metallic Bi nanoparticles buried in an amorphous Li_2O matrix as reported in the literature.^[28,29] The next reversible lithiation and delithiation of the Bi component, *i.e.*, $\text{Bi} + 3\text{Li}^+ + 3\text{e}^- \leftrightarrow \text{Li}_3\text{Bi}$ eventually contribute to lithium storage capacity in successive

[a] K. Tian, H. Lu, L. Bu, X. Huang, S. Yang, Y. Zhao, Prof. J. Zhao, Prof. L. Gao College of Energy, Soochow Institute for Energy and Materials Innovations Soochow University, Suzhou 215006, China
E-mail: jqzhao@suda.edu.cn
gaolijun@suda.edu.cn

[b] K. Tian, H. Lu, L. Bu, X. Huang, S. Yang, Y. Zhao, Prof. J. Zhao, Prof. L. Gao Key Laboratory of Advanced Carbon Materials and Wearable Energy Technologies of Jiangsu Province Soochow University, Suzhou 215006, China

[c] Dr. C.-L. Chiang, Dr. Y.-G. Lin
Materials Science Group, Scientific Research Division, National Synchrotron Radiation Research Center
Hsinchu Science Park, Hsinchu 30076, Taiwan, R. O. C.
E-mail: lin.yg@nsrrc.org.tw

 Supporting information for this article is available on the WWW under <https://doi.org/10.1002/batt.202000108>

electrochemical cycling. Such alloying/de-alloying processes can lead to repetitive volume expansion/shrinkage and considerably accumulated reaction strains within the electrode.^[30] In addition, pulverization of actively reduced Bi particles and severe side reactions also occur during electrochemical lithium storage, which together contribute to fast capacity decay and poor cycling performance of Bi-based anode materials. Rational material engineering and structural design are highly required to stabilize capacity change of oxide-based anode materials during lithiation/de-lithiation processes for prolonged cycling.

Superior lithium storage performance of binary metal oxides has been extensively reported in the literature,^[31–34] owing to synergistic effects between two different oxides during lithiation/de-lithiation processes. For instance, glassy $\text{Bi}_4\text{Ge}_3\text{O}_{12}$ oxide demonstrated high specific capacity and cycling stability as an anode material,^[31] which was attributed to synergistic effects during the conversion and alloying/de-alloying reactions of GeO_2 and Bi_2O_3 oxides, which are two dissociated components of the binary anode material through an initial lithiation. Note that lithium storage mechanism of binary metal oxides in some cases is distinguished from the combination of two single metal oxides. The electrochemical lithium storage behavior of atomically thin Bi_2MoO_6 sheets was different from that in a simple mixture of Bi_2O_3 and MoO_3 oxides.^[32] Metallic Bi and Mo were generated during the initial discharge of Bi_2MoO_6 anode, but only the Bi component was active in lithium storage through alloying/de-alloying reactions in successive cycling. Nevertheless, both conversion and alloying/de-alloying processes during lithiation/de-lithiation of metal oxides could induce deactivation of active anode material and destroy electrode structure upon long-term cycling, due to volumetric changes and accumulated reaction strains.^[35] In order to overcome aforementioned problems and further improve capacity stability of metal oxide anodes, a reliable substrate has to be introduced to accommodate these active metal oxides. The binary $\text{Bi}_2\text{Mo}_3\text{O}_{12}$ metal oxide has been effectively utilized for photocatalytic and electrocatalytic applications,^[36–39] but, to the best of our knowledge, it is still unexplored as a potential anode material for Li-ion batteries. One motivation of research is due to its attractively high theoretical capacity of 900 mAh g^{-1} .

In this work, *in-situ* synchrotron X-ray diffraction (XRD) measurements were carried out to explore lithium storage mechanism of $\text{Bi}_2\text{Mo}_3\text{O}_{12}$ (BMO) binary metal oxide in a voltage range of 0.01–3.0 V vs. Li^+/Li , coupled with voltage-resolved cyclic voltammetry (CV) and *ex-situ* X-ray photoelectron spectroscopy (XPS) analyses. Moreover, through *in-situ* compositing with Ti_3C_2 -based MXene nanosheets as support, $\text{Bi}_2\text{Mo}_3\text{O}_{12}/\text{Ti}_3\text{C}_2$ (BMO@TC) composite anode material shows enhanced cycling stability and rate capability compared with bare $\text{Bi}_2\text{Mo}_3\text{O}_{12}$ and carbon-coated $\text{Bi}_2\text{Mo}_3\text{O}_{12}/\text{C}$ (BMO@C) for prolonged cycles. The findings from this work provide some insights into rational design of new metal oxide-based anode materials and associated composite nanostructures for high-performance Li-ion batteries.

2. Results and Discussion

Morphological and structural characteristics of as-prepared BMO material were examined by SEM/TEM observations. As shown in Figure 1a, the FESEM image reveals spherically-shaped and highly-dispersed features of secondary BMO particles with an average particle size of 150 nm. The TEM image indicates the compact assembly of numerous primary nanoparticles in a single BMO nanosphere (Figure 1b), and EDS element mappings in the STEM mode verify uniform distributions of Bi, Mo and O elements within each secondary particle (Figure 1c). Structural characteristics of primary BMO nanoparticles are displayed in the HRTEM image (Figure 1d) that was captured on the selected area noted in Figure 1b by the yellow square. Note that all primary particles are highly-crystallized monocrystals with an even particle size of approximately 5 nm. In addition, Figure 1e shows the TEM image of carbon-coated BMO@C material, revealing that secondary BMO nanospheres are all expectedly encased within a carbon matrix. XRD patterns of BMO and BMO@C samples are identical as compared in Figure 1f, which can be well indexed to a monoclinic α - $\text{Bi}_2\text{Mo}_3\text{O}_{12}$ phase with the space group of P2₁/c (JCPDS: 21-0103), in consistence with that reported in the literature.^[40] Additionally, XRD results also imply an amorphous texture or a low graphitization degree of carbon component within the BMO@C material, probably due to the low reaction temperature during hydrothermal synthesis. Lattice fringes in HRTEM image with measured interplanar spacings of 3.34, 2.63 and 2.35 Å correspond to (210), (221) and (231) planes of resulting BMO monocrystals (Figure 1d). To explore chemical environment and valence states of different elements in BMO and carbon-coated BMO@C materials, XPS survey spectra and associated high-resolution Bi 4f, Mo 3d, O 1s and C 1s XPS spectra were recorded on the two samples as plotted in Figure S1, 1g and 1h, respectively. Characteristic Mo 3d_{3/2} and 3d_{5/2} peaks of the two materials are both centered at binding energies of 236.4 and 233.3 eV, respectively, indicating the hexa-valent Mo⁶⁺ state of the BMO and BMO@C. The BMO@C shows broadened Mo 3d peaks, as analyzed by the deconvolution treatment (the bottom panel in Figure 1h), which can be attributed to the Mo–C bonding formed during hydrothermal carbon coating process.^[41] It is seen from the C 1s XPS spectra of BMO and BMO@C samples that the bonds of carbon (O–C=O, C–O, C–C) are almost identical for the two samples (Figure S1a), the carbon on BMO may be originated from the surfactant CTAB during hydrothermal process. The same happens to the O 1s XPS spectra that nearly no difference is found for the BMO and BMO@C samples (Figure S1b). On the other hand, two samples present identical Bi 4f_{5/2} and Bi 4f_{7/2} peaks centered at 165.4 and 160.1 eV, respectively (Figure 1g), revealing the tri-valent Bi³⁺ state. Briefly, material characterizations through XRD, TEM and XPS measurements certify the successful preparation of BMO binary metal oxide and its carbon-coated derivative.

In order to understand lithium storage mechanism of this unexplored BMO, *in-situ* synchrotron XRD measurements were performed on the BMO anode during lithiation/de-lithiation processes in a voltage range of 0.01–3.0 vs. Li^+/Li , coupled with

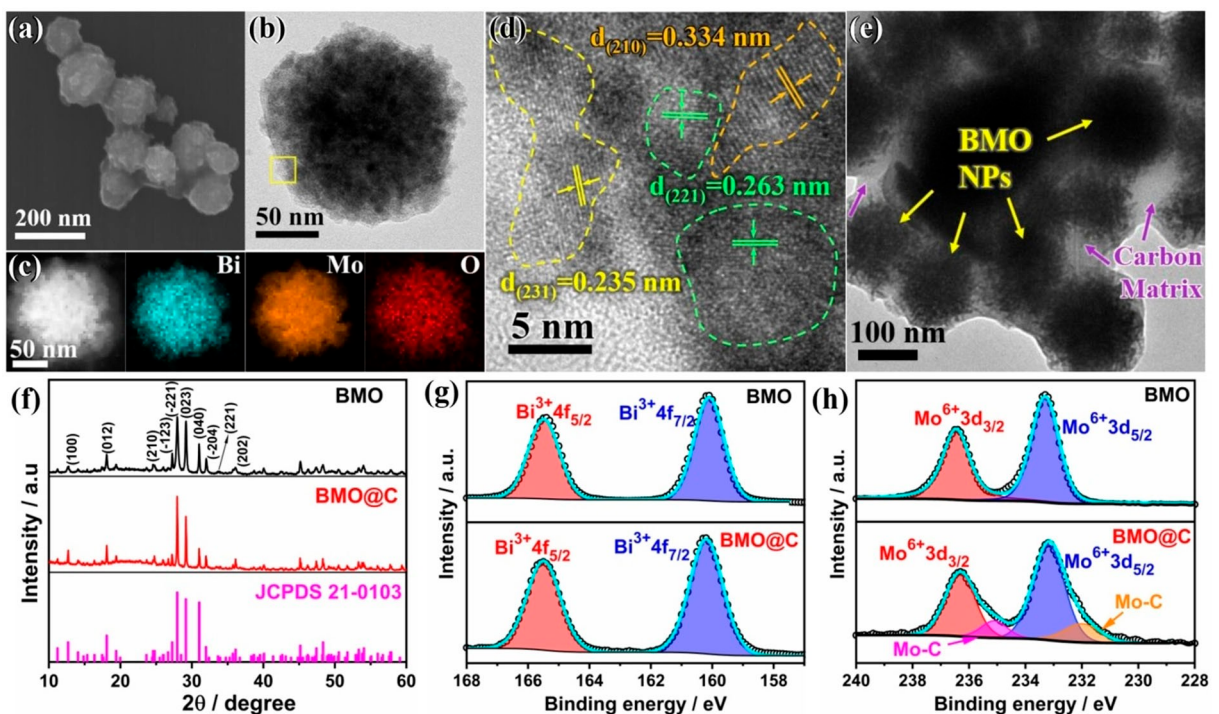


Figure 1. a) FESEM image, b) TEM image, c) EDS mappings in the STEM mode and d) HRTEM image of BMO material. e) TEM image of BMO@C material. f) XRD patterns, g) Bi 4f XPS peaks and h) Mo 3d XPS of two samples.

preliminary CV analysis. Figure 2a plots CV profiles in the first three cycles at a scanning rate of 0.1 mV s^{-1} . Several cathodic and anodic peaks can be identified in CV curves, indicating lithium storage activities of the BMO electrode. During initial lithiation, a first cathodic CV peak appears at 2.07 V with a high current density, which is attributed to the irreversible conversion reaction of BMO into metallic Bi and MoO_δ oxide. The second cathodic peak is localized at 1.36 V, together with a shoulder peak at 1.31 V, responding to the Li-ion intercalation into MoO_δ component to form $\text{Li}_x\text{MoO}_\delta$ intermediate.^[32] This is in agreement with the literature^[17,42,43] that the two CV peaks may be due to the two-step intercalation process or phase transition of lithiated $\text{Li}_x\text{MoO}_\delta$ intermediate of Mo-based oxides. The broad cathodic peak centered at 0.61 V can be attributed to the alloying of reduced Bi to form Li_3Bi through continuous and deep lithiation.^[32,44] The sharp current response below 0.5 V is resulted from the formation of a solid electrolyte interface (SEI) film at electrode surface. In the subsequent delithiation process on reverse voltage scan from 0.01 to 3.0 V, only two wide anodic peaks were recorded and centered at approximately 1.0 and 1.6 V. The former is attributed to the de-alloying of Li_3Bi to metallic Bi, and the latter can be assigned to the de-lithiation of $\text{Li}_x\text{MoO}_\delta$ to regain MoO_δ component. In the next CV cycles, Li-ion intercalation/de-intercalation processes in MoO_δ component result in a redox couple of broad reduction and oxidation peaks at approximately 1.16 and 1.62 V, respectively. Moreover, alloying/de-alloying reactions of Bi component account for the other redox pair of reduction and oxidation peaks located at around 0.58 and 1.06 V, respectively. CV curves in the second and third cycles are highly overlapped,

indicating desired electrochemical reversibility of these two lithium storage reactions. Note that the sharp cathodic peak at low voltages is still present, which implies the continuous formation of SEI film during cycling.

In-situ synchrotron XRD measurements were then carried out to clarify lithium storage behaviors of the BMO anode. Figure 2b presents *in-situ* XRD patterns recorded during initial lithiation/de-lithiation processes at a current density of 100 mA g^{-1} , which are as a function of discharging and charging voltages marked in different colors, along with corresponding discharge/charge curves (Figure 2b-I) and a zoom-in view between 9.2 and 9.6° (Figure 2b-III). In addition, Figure 2c presents two-dimensional contour plots of *in-situ* XRD peak intensities at different selected 2θ ranges. During the initial discharge starting from open circuit voltage (OCV), the BMO anode material shows gradually decreased intensities of $(012)_{\text{BMO}}$, $(-121)_{\text{BMO}}$, $(-113)_{\text{BMO}}$, $(210)_{\text{BMO}}$, $(-221)_{\text{BMO}}$, $(023)_{\text{BMO}}$, $(040)_{\text{BMO}}$ and $(-204)_{\text{BMO}}$ reflections (Figure 2c). These diffraction peaks all disappear at approximately 1.82 V, indicating the complete conversion of original $\text{Bi}_2\text{Mo}_3\text{O}_{12}$ at this voltage upon continuous lithiation. Meanwhile, a new diffraction peak appears at $2\theta = 12.1^\circ$ (Figure 2c-IV) after 1.82 V, which can be indexed to the (012) reflection of metallic Bi (JCPDS No.: 44-1246). The Mo-based phase, *i.e.*, Li_2MoO_4 (JCPDS No.: 12-0763) is detectable at a lower voltage of $\sim 1.05 \text{ V}$, according to the characteristic $(221)_{\text{LMO}}$ reflection at $2\theta = 9.4^\circ$ (Figure 2c-II). *In-situ* XRD results coupled with CV analysis suggest that irreversible conversion of BMO into metallic Bi and Li_2MoO_4 occurs through electrochemical lithiation, in consistence with *ex-situ* XRD measurement results at B and C marked spots (Figure S2a and

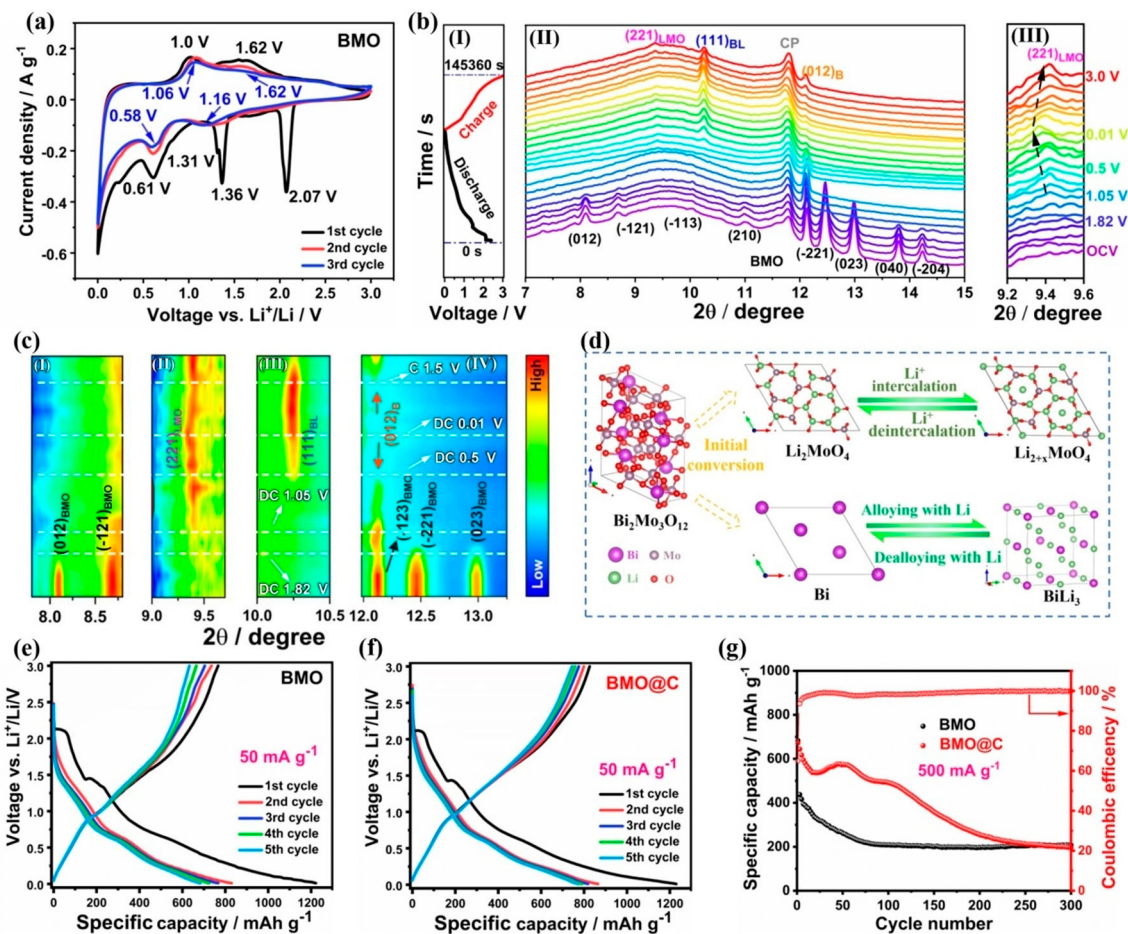
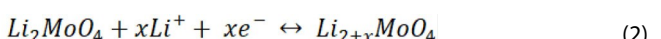
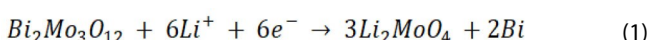


Figure 2. a) CV curves in the first three cycles recorded at a scanning rate of 0.1 mV s⁻¹, b) *in-situ* synchrotron XRD measurements during initial lithiation/delithiation processes of BMO anode: I) recorded charge/discharge curves, II) *in-situ* XRD patterns at different charge/discharge voltages and III) zoom-in view between 9.2 and 9.6°, along with c) corresponding contour plots of *in-situ* XRD peak intensities (marked in colors from low in blue and red in high intensity) in several selected 2θ ranges I-IV) and d) schematics illustrating the lithium storage reaction mechanism. Charge/discharge curves in the first five cycle of e) BMO and f) BMO@C anode materials at 50 mA g⁻¹ in a voltage range of 0.01–3.0 V vs. Li⁺/Li, and g) cycling performance at 500 mA g⁻¹ upon 300 cycles.

S2b). Upon continuous lithiation to lower voltages, the (111)_{BL} reflection of Li₃Bi appears at $2\theta = 10.25^\circ$ (JCPDS No.: 12-0763) when discharged below 0.5 V as it is shown in Figure 2c-III, revealing the alloying reaction of Bi component with Li-ion to form Li₃Bi alloy. In addition, the zoom-in pattern view between 9.2 and 9.6° as shown in Figure 2b-III reveals continuous peak shift of the (221)_{LMO} reflection to the lower 2θ position till the end of discharge, implying an unexpected intercalation of excessive Li-ion into the Li₂MoO₄ component to form Li_{2+x}MoO₄ derivative at 0.01 V. Accordingly, *ex-situ* XRD pattern at the D spot (Figure S2a and S2b) confirms the electrochemical and chemical stability of Li_{2+x}MoO₄ phase, because it was measured on the cycled electrode stopped at 0.01 V that was disassembled from deeply-discharged coin cell and then exposed to the air during *ex-situ* measurements. However, the supposed Li₃Bi alloy was not detected at the D spot, and instead, a cubic Bi phase was detected. This is different from the observation in *in-situ* synchrotron XRD measurement (Figure 2c-III and 2b-II) where the Li₃Bi phase is clearly identified from the (111)_{BL} reflection at $2\theta = 10.25^\circ$. The possible reason is that the highly active Li metal within Li₃Bi alloy was burned in the air during

ex-situ measurements, leaving the cubic Bi phase that has the same structural configuration as that of Li₃Bi. Furthermore, the conversion of BMO into Bi and Li₂MoO₄ leads to distinct binding energy difference of -0.9 eV and -1.0 eV in *ex-situ* high-resolution Bi 4f and Mo 3d XPS peaks between A and B spots (Figure S2c and S2d), respectively, owing to the changed chemical environment of Mo element and reduced valence state of Bi element. The successive peak shifts of Mo 3d (232.3 to 232.1 eV) and Bi 4f (159.0 to 158.6 eV) in XPS spectra to lower binding energies from B to D spots can be attributed to the continued lithiation of two converted components, *i.e.*, Li-ion intercalated into Li₂MoO₄ and alloyed with Bi, in well concurrence with *in-situ* and *ex-situ* XRD results. Similar behavior on binding energy changes from 54.9 to 55.2 eV (B to D) of high-resolution Li 1s XPS peaks in *ex-situ* XPS can be observed (Figure S2e). During the subsequent charging process from 0.01 to 3.0 V, the (111)_{BL} reflection shows gradually decreased intensity upon delithiation (Figure 2c-III). Meanwhile, the (012)_B reflection of metallic Bi is re-detected (Figure 2c-IV) after 1.5 V, indicating a reversible dealloying of Li₃Bi to the reformation of Bi. Concurrently, the (221)_{LMO} reflection gradually

retrieves to the initial 2θ position with increased intensity (Figure 2b-III and 2c-II), which indicates a reversible Li-ion de-intercalation from $\text{Li}_{2+x}\text{MoO}_4$ to regain the Li_2MoO_4 component. *Ex-situ* XRD patterns at E and F spots (Figure S2a) also verify the presence of Bi and Li_2MoO_4 phases (Figure S2b). In addition, characteristic Mo 3d and Bi 4f peaks both shift back to higher binding energies from D to F spots in *ex-situ* XPS spectra as presented in Figure S2c and S2d. Note that binding energies of both Mo 3d XPS peak and Bi 4f XPS peak at F spot are correspondingly equal to that at B spot, suggesting identical chemical environment and valence states of Mo and Bi elements after a lithiation/delithiation cycle from B to F spots. Briefly, *operando* XRD results coupled with *ex-situ* XRD and XPS examinations certify that electrochemically reversible reactions of Bi and Li_2MoO_4 components take place for lithium storage after 1.8 V. On the basis of above CV, XRD and XPS analyses, an electrochemical lithium storage mechanism of BMO anode material is suggested as following:



Notably, as illustrated in schematics in Figure 2d, the BMO anode undergoes an irreversible conversion reaction generating unique Li_2MoO_4 and commonly-reported metallic Bi through initial lithiation [Equation (1)]. This observation is different from that of the binary metal oxide Bi_2MoO_6 reported in the literature.^[32] The completely suppressed reduction of Mo^{6+} ions to lower valence states during the initial discharge process may be attributed to the enhanced electronic conductivity of Mo-based component by mixing with metallic Bi component. Such an observation is also to some extent confirmed by comparing Mo 3d XPS peaks of MoO_3 and $\text{MoO}_3@30\%$ CNTs (*i.e.*, MoO_3 mixed with 30 wt.% of conductive carbon nanotubes) anode materials highly-discharged to 0.01 V vs. Li^+/Li . As shown in Figure S4, the deeply-lithiated $\text{MoO}_3@30\%$ CNTs anode reveals reduced intensity of Mo^0 3d XPS peaks at the binding energies of 229 and 232 eV in contrast to that of bare MoO_3 material. The CNTs may play the same role as that of Bi metal in impeding the reduction of Mo^{6+} into Mo^0 by offering high conductivity for fast charge transfer in MoO_3 anode, thus the conversion reaction to Mo metal is effectively suppressed. Moreover, the Li_2MoO_4 component experiences uptake and release of extra Li-ions driven by electrochemical intercalation/de-intercalation [Equation (2)], which eventually contributes to reversible lithium storage capacity, corresponding to the redox pair at approximately 1.16/1.62 V in the third CV cycle (Figure 2a). In addition, the existence of metallic Bi in the composite may favor lithium storage kinetics due to the increased conductivity. At low voltages Bi is transitioned into alloyed Li_3Bi , and the reaction is

reversible [Equation (3)], which contributes to total electrode capacity. In order to confirm the above proposed lithium storage mechanism, *ex-situ* XRD patterns of cycled BMO anode material were further measured at fully-charged (to 3.0 V vs. Li^+/Li) and -discharged (to 0.01 V vs. Li^+/Li) conditions after several electrochemical cycles. As shown in Figure S3a, cycled BMO anode material at deeply charged/discharged situations both show characteristic diffraction peaks belong to the Li_2MoO_4 (LMO) phase, and slight peak shift can also be found in the zoom-in view (Figure S3b), in consistence with *in-situ* synchrotron XRD measurements during initial lithiation/de-lithiation in the first cycle. The absence of Li_3Bi phase at 0.01 V may be attributed to the formation of ultrafine Li_3Bi nanoparticles in low crystallinity after prolonged cycling, which is out of detectable capability by *ex-situ* powder XRD measurement, while the metallic Bi phase was detected at 3.0 V. Overall, such *ex-situ* XRD results highly complement to *in-situ* synchrotron XRD measurements, and thus verify the proposal of reversible lithium storage of Li_2MoO_4 and Bi components as suggested in Equation (2) and (3) for long-term electrochemical cycling.

Lithium storage electrochemical performance of the BMO anode material was then evaluated in a voltage range of 0.01–3.0 V vs. Li^+/Li . Figure 2e plots charge/discharge curves in the first five cycles at a low current density of 50 mA g⁻¹. The BMO anode can deliver attractive initial discharge and charge capacities of 1222 and 766 mAh g⁻¹, respectively. Taking the initial charge capacity of 766 mAh g⁻¹ as the theoretical capacity, which involves contribution from Bi alloying and Li_2MoO_4 intercalation reactions, the x value in $\text{Li}_{2+x}\text{MoO}_4$ can be calculated to be approximately 2.5 (SI calculation). However, the oxide-based anode materials typically suffers from capacity fading and poor cycling stability, especially under high current densities, owing to repetitive volume expansion/contraction and considerably accumulated strains through conversion, intercalation/de-intercalation and alloying/de-alloying reactions for lithium storage.^[33] As presented in Figure 2g, the BMO anode shows an inferior 30% capacity retention at 500 mA g⁻¹ upon 300 cycles, which is probably due to complex lithium storage behaviors [Equations (1)–(3) and Figure 2d]. In order to improve lithium storage performance, a conventional strategy of carbon coating was adopted on BMO nanoparticles. TEM image shown in Figure 1e verifies that all secondary BMO nanospheres were encased within a high-quality carbon matrix. In addition, the BMO@C anode shows identical CV curves as that of BMO in the first three cycles (Figure S5 and 2a), indicating the same lithium storage behaviors after carbon coating. The carbon coating indeed results in increased lithium storage capacity and enhanced cycling stability of BMO@C compared with BMO anode at 50 mA g⁻¹ (Figure 2f). The BMO@C retains a desired charge capacity of 775 mAh g⁻¹ in the fifth cycle, higher than that of BMO (677 mAh g⁻¹). However, the carbon-coated BMO anode still encounters rapid capacity decay after 100 cycles at high current density of 500 mA g⁻¹ (Figure 2g), which probably can be attributed to the poor structural stability of carbon matrix. Hence, rational structural design of BMO anode material with a reliable substrate is

highly required to improve cycling stability for prolonged cycles.

Two-dimensional MXene materials have been demonstrated as the versatile supporters for various functional materials to boost their electrochemical performance in device applications, because of their superior electronic conductivity, robust structural stability and remarkable chemical durability.^[45–49] In order to ameliorate cycling stability of BMO anode material, a typical Ti_3C_2 -based MXene material was employed as the composite substrate. Schematics in Figure 3a illustrate the *in-situ* hydrothermal preparation of $\text{Bi}_2\text{MoO}_4@\text{Ti}_3\text{C}_2$ (BMO@TC) composite material. As reported in the literature,^[50] Ti_3C_2 (marked as TC) stacks can be obtained after etching the Al layer within commercial Ti_3AlC_2 MAX

powders in an acidic HF solution, resulting in typical accordion-like multilayers as presented in Figure S6. Plenty of hydroxyl groups were concurrently generated at the surface during etching process, which accounts for excellent hydrophilic property of the TC material. In addition, XPS survey spectrum and high-resolution Ti 2p and C 1s XPS peaks captured on collected TC stacks are highly consistent with those reported in the literature,^[51,52] indicating the successful preparation of Ti_3C_2 -based MXene material. Further exfoliation of functionalized TC stacks via high-energy ultrasonication treatment effectively produced well-dispersed TC nanosheets in an aqueous solution, which show desired monolayer characteristics as examined by TEM observation in Figure S7. The hydrothermal reaction was carried out on the mixed solution with uniformly-dispersed TC

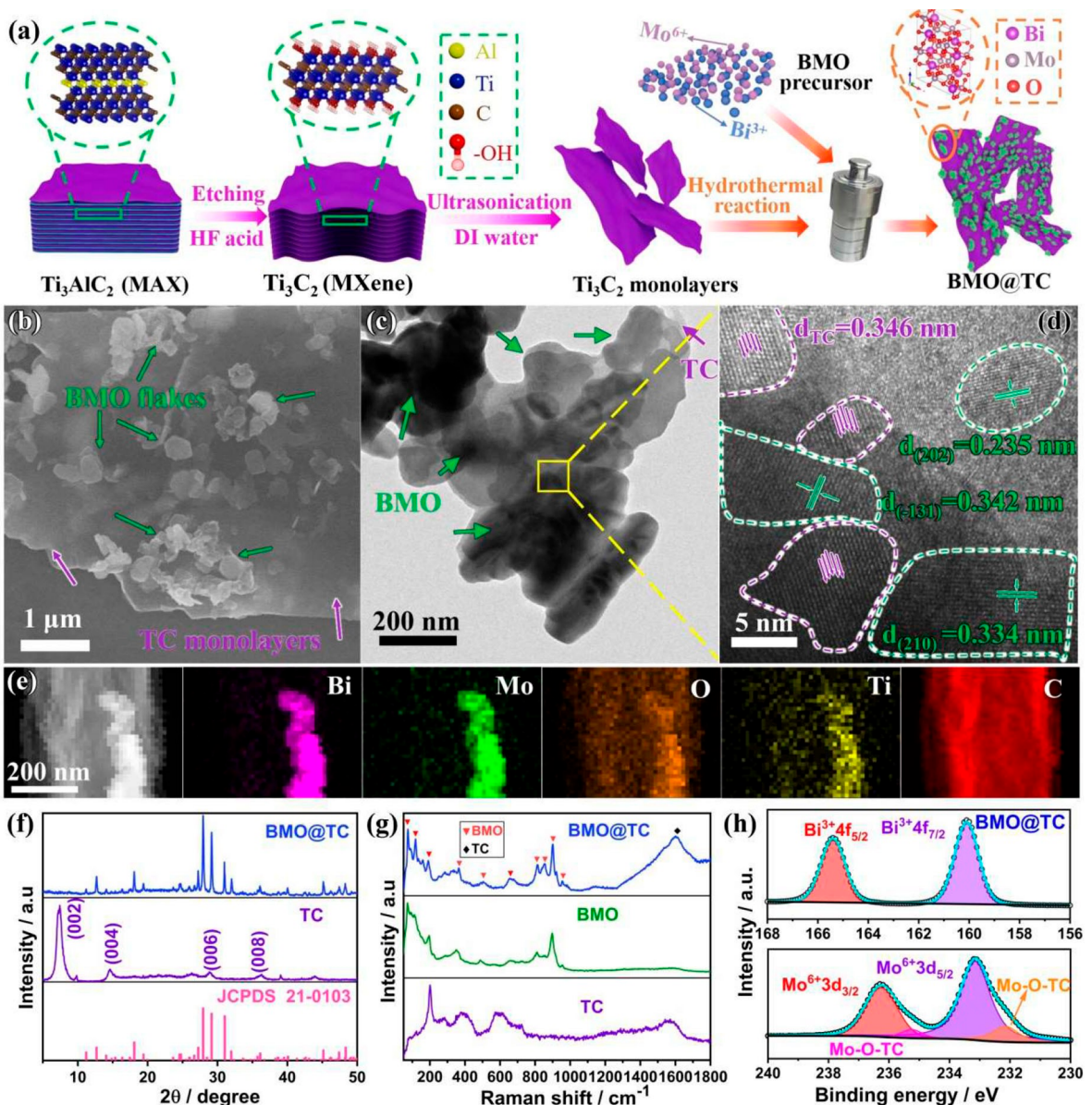


Figure 3. a) Schematics illustrating the preparation process of BMO@TC composite material, together with b) FESEM image, c) TEM image, d) HRTEM image and e) EDS element mappings in the STEM mode. f) XRD patterns of TC and BMO@TC samples. g) Raman spectra captured on TC, BMO and BMO@TC samples. h) High-resolution Bi 4f and Mo 3d XPS peaks of BMO@TC material, coupled with deconvolution treatment.

nanosheets and dissolved Bi/Mo precursors to obtain the MXene-supported BMO composite material (Figure 3a). Morphological and structural characteristics of resulting BMO@TC nanocomposite are presented in Figure 3b–e. FESEM and TEM images reveal flake-shaped BMO particles with an average particle size of approximately 200 nm, which are anchored on micron-sized transparent TC monolayers (Figure 3b and 3c). Notably, the BMO flakes are apparently different in morphology from the secondary nanospheres of BMO samples (Figure 1a and 1b), probably due to the replica growth following the two-dimensional layer-structured TC substrate during hydrothermal synthesis. Furthermore, in order to examine the local structure features, HRTEM image was captured near a central area of the BMO@TC sheet from Figure 3c (the selected area in yellow square) and shown in Figure 3d, the TC substrate can be identified by the unique lattice fringe with an interplanar crystal spacing of 3.46 Å. Note that these planes are discrete, which is probably attributed to the partial coverage of some BMO flakes at the surface of TC nanosheet. In addition, the HRTEM image also reveals single crystal structure of BMO flakes in high crystallinity, $(202)_{\text{BMO}}$, $(-131)_{\text{BMO}}$ and $(210)_{\text{BMO}}$ planes can be indexed on the basis of different clear lattice fringes of 0.235, 0.342 and 0.334 nm, respectively. Figure 3e shows EDS element mappings collected on the BMO@TC composite material in STEM mode, which again verify the anchoring of BMO particles on the surface of TC substrate, according to distinguishable signal distributions among Bi, Mo, O, Ti and C elements. As shown in Figure 3f, the diffraction XRD peaks of BMO@TC composite are equivalent to those obtained from pure BMO (JCPDS: 21-0103). However, the TC component cannot be detected in the XRD pattern of BMO@TC material, probably due to the small mass amount of TC in the BMO@TC. While the pure TC film that was obtained through filtrating dispersion solution of TC nanosheets shows dominant characteristic (002) reflection positioned at $2\theta = 7.5^\circ$.^[50] It can thus be inferred that the presence of TC nanosheets had little effect on the crystal structure of the BMO. By contrast, the Raman spectrum of BMO@TC sample contains all characteristic peaks from both BMO and TC components as shown in Figure 3g. The Raman spectrum of BMO confirms the coordination environment and dominant modes corresponding to bond stretches from the MoO_5 species,^[53] resulting in characteristic peaks located at 954, 914, 899 and 856 cm⁻¹. Another three peaks positioned at 398, 310, and 242 cm⁻¹ combine Mo–O stretches in the MoO_5 and Bi–O stretches in different bending, wagging and external modes. Additionally, the broad peak centered at 1566 cm⁻¹ in the BMO@TC sample results from the D band effect of the TC component.

High resolution Bi 4f and Mo 3d XPS spectra were also recorded to probe possible chemical bonds between BMO flakes and TC substrate. As shown in Figure 3h, the BMO@TC composite material shows identical Bi 4f XPS spectrum to that of BMO sample (Figure 1f), resulting in two Bi 4f_{5/2} and 4f_{7/2} peaks centered at 165.4 eV and 160.1 eV, respectively. Note that Mo 3d_{3/2} and 3d_{5/2} peaks become notably wider in contrast to that of BMO sample (Figure 1e), which can be attributed to an additional Mo–O–TC bonding effect based on the convolution treatment,

and thus imply the formation of favorable covalent bond interaction between BMO flakes and the TC support through hydroxyl (OH) group at the surface of TC nanosheets.

Accordingly, Figure 4 shows the evaluation of MXene-supporting effect on boosting lithium storage performance of BMO anode material. The BMO@TC composite anode shows very similar responses of cathodic and anodic peaks in CV records in the first three cycles as that of BMO anode (Figure 4a and 2a), implying unchanged lithium storage behaviors from the active BMO component in BMO@TC. Notably, the BMO@TC composite displays apparently increased peak intensities of two reversible redox pairs at 0.49/1.14 and 1.19/1.73 V in the third CV curve, indicating enhanced lithium storage activities of Bi and Li_2MoO_4 components at the surface of TC substrate. Charge/discharge curves of the BMO@TC anode in the first five cycles at 50 mA g⁻¹ are plotted in Figure 4b. It delivers an initial charge capacity of 846 mA h g⁻¹, which is higher than that of BMO (766 mA h g⁻¹) and carbon-coated BMO@C (826 mA h g⁻¹) anode materials shown in Figure 2e and 2f, respectively. Moreover, the TC MXene support also plays a significant role in improving cycling stability and rate capability at high current densities for the BMO@TC anode. As presented in Figure 4c, the BMO@TC anode can retain an impressive capacity of 512 mA h g⁻¹ after 300 cycles at 500 mA g⁻¹, more than twice that of preserved capacities of cycled BMO and BMO@C after the same prolonged period of cycling (Figure 2g). Note that the capacity remains nearly unchanged after experiencing some decays in initial ten cycles, revealing desired structural stability of the MXene-supported composite material. The initial capacity fading can probably be attributed to the formation of SEI film on the electrode surface, especially at large surface of porous TC nanosheets. TC also makes some contribution to lithium storage capacity (~90 mA h g⁻¹), due to Li-ion intercalation into interlayers and interaction with surface functional groups of Ti_3C_2 MXene. Figure 4d compares high-rate performance among four different anode materials after cycling at 50 mA g⁻¹ for five cycles. As compared with BMO and carbon-coated BMO@C materials, the BMO@TC composite exhibits considerably increased capacities of 696, 605, 532, 436 and 269 mA h g⁻¹ at current densities of 0.1, 0.25, 0.5, 1 and 2.5 A g⁻¹, respectively. When returning to a low 0.1 A g⁻¹ charge/discharge current, the BMO@TC is able to regain and retain its high capacity close to 700 mA h g⁻¹, indicating desired lithium storage kinetics and electrochemical reversibility. TC shows a little capacity contribution but its role is mainly as a conductive substrate support. Moreover, Figure 4e shows cycling performance of BMO@TC anode under 2.5 A g⁻¹ high charge/discharge current density for 1000 cycles, a satisfied capacity of approximately 227 mA h g⁻¹ can be obtained after such a long cycle.

Figure S9 shows EIS spectra BMO@TC anode material measured at open circuit voltage in the initial state (i.e. fresh electrode) and after 50 cycles (cycled electrode). According to the simulation result from an equivalent circuit (insets in Figure S9), the fresh BMO@TC shows a smaller charge-transfer resistance ($R_{ct} = 65.6 \Omega$) compared with that of cycled BMO@TC

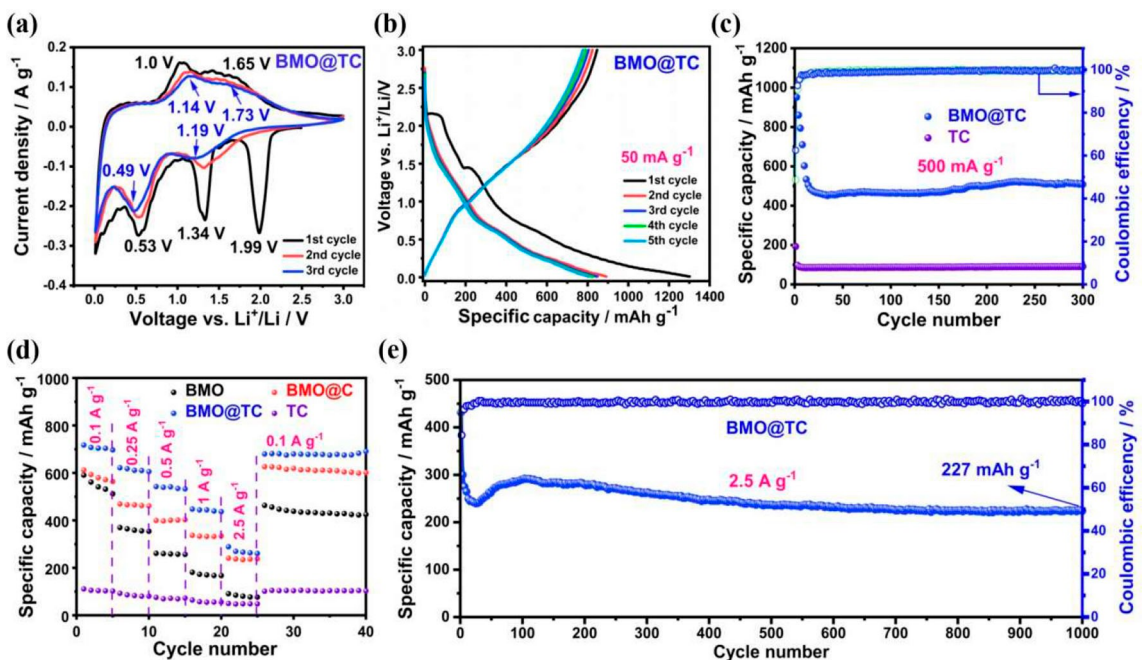


Figure 4. Electrochemical performance of BMO@TC composite anode material: a) CV curves in the first three cycles recorded at a scanning rate of 0.1 mV s^{-1} , b) charge/discharge curves in the first five cycle at 50 mA g^{-1} in a voltage range of $0.01\text{--}3.0 \text{ V}$ vs. Li^+/Li , c) cycling performance at 500 mA g^{-1} compared with the TC anode, d) high-rate performance up to 2.5 A g^{-1} compared with BMO, carbon-coated BMO@C and TC anodes, and e) cycling performance at 2.5 A g^{-1} for prolonged 1000 cycles.

($R_{ct}=412.5 \Omega$), indicating that the charge transfer reaction kinetics across the electrode/electrolyte interface becomes sluggish after cycles.

Additionally, the two cycled anode materials were examined by TEM observations as presented in Figure S10. The TEM image of cycled BMO@TC anode material shows well-preserved structure in comparison with the original composite material (Figure S10a and 3c). However, the cycled BMO material reveals distinct structural difference from original spherical secondary particle (Figure S10b and 1b). After cycles the BMO shows porous flower-like shape consisting of many needles. This structural change of BMO after cycling can be attributed to drastic volumetric changes and accumulated reaction strains upon cyclic lithiation/de-lithiation processes.^[35] Enhanced cycling and high-rate performance of the BMO@TC anode material can be attributed to improved structural stability enabled by TC MXene supporting substrate. The results indicate that synergistic combination of binary components, particularly with the presence of metallic Bi and Li_2MoO_4 intermediates, can have significant effects on improving electrochemical performance of such a $\text{Bi}_2\text{Mo}_3\text{O}_{12}$ binary anode material.

3. Conclusions

Lithium storage performance was explored on the $\text{Bi}_2\text{Mo}_3\text{O}_{12}$ binary metal oxide as an anode material for Li-ion batteries. Associated lithium storage mechanism was comprehensively elucidated on the basis of *in-situ* synchrotron XRD probing during initial lithiation/de-lithiation processes, coupled with CV

profiles analysis and voltage-resolved *ex-situ* XPS and XRD measurements. The $\text{Bi}_2\text{Mo}_3\text{O}_{12}$ anode material undergoes an irreversible conversion reaction forming Li_2MoO_4 and metallic Bi phases upon initial lithiation process. Lithium storage capacity delivered in successive electrochemical cycling is believed to be originated from two reversible reactions, one is the alloying/de-alloying between Bi and Li_2Bi , and the other is the intercalation/de-intercalation between Li_2MoO_4 and $\text{Li}_{2+x}\text{MoO}_4$. In an effort to ameliorate cycling stability of $\text{Bi}_2\text{Mo}_3\text{O}_{12}$ anode, Ti_3C_2 -based MXene nanosheets were employed as the supporting substrate. The $\text{Bi}_2\text{Mo}_3\text{O}_{12}/\text{Ti}_3\text{C}_2$ composite material was prepared in a hydrothermal reaction, in which flake-shaped $\text{Bi}_2\text{Mo}_3\text{O}_{12}$ particles were anchored at the surface of Ti_3C_2 monolayers. The $\text{Bi}_2\text{Mo}_3\text{O}_{12}/\text{Ti}_3\text{C}_2$ composite anode material can deliver an initial charge capacity of 846 mAh g^{-1} at 50 mA g^{-1} and retain 227 mAh g^{-1} capacity upon prolonged 1000 cycles at 2.5 A g^{-1} high charge/discharge current density, which demonstrates significantly enhanced cycling stability and rate capability compared with that of bare $\text{Bi}_2\text{Mo}_3\text{O}_{12}$ and carbon-coated $\text{Bi}_2\text{Mo}_3\text{O}_{12}/\text{C}$ anode materials. The findings from this study provide some insights into developing new binary metal oxide-based anode materials, together with rational structural design and material engineering towards enhanced lithium storage performance for Li-ion battery applications.

Experimental Section

Synthesis of $\text{Bi}_2\text{Mo}_3\text{O}_{12}$ and carbon-coated $\text{Bi}_2\text{Mo}_3\text{O}_{12}@\text{C}$ materials

The $\text{Bi}_2\text{Mo}_3\text{O}_{12}$ material was prepared using a hydrothermal method. 265 mg $(\text{NH}_4)_4\text{Mo}_7\text{O}_{24} \cdot 4\text{H}_2\text{O}$ was dissolved in 5 mL deionized (DI) water under continuous ultrasound to form the Mo precursor solution. Meanwhile, 243 mg $\text{Bi}_2(\text{NO}_3)_3 \cdot 5\text{H}_2\text{O}$ was dissolved in 5 mL Ethylene Glycol (EG) to form the Bi precursor solution. The above two solutions were then added into the surfactant solution, *i.e.*, 30 mg cetyl trimethyl ammonium bromide (CTAB) dissolved in 30 mL DI water, followed by sonicating for extra 20 min. The resulting solution was then transferred to a 50 mL autoclave and heated at 180 °C for 24 h. After cooling to the room temperature, dark precipitate was collected and washed with DI water and ethanol alternatively for several times. The $\text{Bi}_2\text{Mo}_3\text{O}_{12}$ (marked as BMO) powder was obtained after drying at 80 °C for 24 h. In order to coat the carbon layer on BMO particles, 200 mg glucose was dissolved in 30 mL DI water to disperse 200 mg BMO powder under continuous stirring. The mixed solution was transferred to a 50 mL autoclave and heated at 180 °C for 4 h. After cooling to the room temperature, dark precipitate was collected and washed with DI water and ethanol alternatively for several times. The carbon-coated $\text{Bi}_2\text{Mo}_3\text{O}_{12}@\text{C}$ (marked as BMO@C) powder was obtained after drying at 80 °C for 24 h.

Synthesis of MXene-supported $\text{Bi}_2\text{Mo}_3\text{O}_{12}@\text{Ti}_3\text{C}_2$ composite materials

Ti_3C_2 -based MXene nanosheets were obtained through etching the Al layer within the Ti_3AlC_2 MAX powder. 2 g LiF was added into 40 mL HCl solution at a high concentration of 9 M to form the HF solution. 2 g Ti_3AlC_2 powder was then very slowly added into the above acidic solution for at least 5 min in order to avoid the overheating during this strong exothermic reaction. The etching process was carried out at 35 °C under continuous stirring for 24 h. The resulting Ti_3C_2 nanosheets were collected and washed with DI water for several times until the pH value of the Ti_3C_2 solution reached to neutral at 7. Ti_3C_2 monolayers were exfoliated through sonicating the obtained Ti_3C_2 solution for 2 h under N_2 protection. The MXene-supported $\text{Bi}_2\text{Mo}_3\text{O}_{12}@\text{Ti}_3\text{C}_2$ composite material was *in-situ* prepared using a hydrothermal method. 30 mg cetyltrimethylammonium bromide (CTAB) and 10 ml Ti_3C_2 solution at a concentration of 3 mg/mL were mixed in 20 mL DI water uniformly, followed by adding the same Mo and Bi precursor solutions for the synthesis of BMO material. After sonicating for 20 min, the mixed solution was then transferred to a 50 mL autoclave and heated at 180 °C for 24 h. After cooling to room temperature, dark precipitate was collected and washed with DI water and ethanol alternatively for several times. The $\text{Bi}_2\text{Mo}_3\text{O}_{12}@\text{Ti}_3\text{C}_2$ (marked as BMO@TC) powder was obtained by freeze drying at -55 °C for 24 h.

Material characterizations

元素在不同材料中的特性通过 X 射线光电子能谱 (XPS) 进行表征，使用 ESCALAB 250Xi XPS 仪器 (Thermo Fisher)。所有 XPS 光谱都已校准，根据 C 1s 峰在 284.8 eV 处的结合能。Raman 光谱在不同的材料上使用 Horiba Jobin Yvon HR Evolution 633 nm 激光进行，而 Fourier 变换红外 (FTIR) 光谱则在 Tensor 27 FTIR 分析仪上记录。

In-situ synchrotron XRD measurements of coin cells with $\text{Bi}_2\text{Mo}_3\text{O}_{12}$ electrode

在不同电压下的原位同步辐射 XRD 实验在台湾光源站 (TLS 01C2) 中进行，位于国家同步辐射研究设施，新竹，台湾。带有针孔的硬币电池在两个透明 Kapton 胶带 (1.0 × 1.0 cm²) 上粘贴，以便 X 射线束能够通过线圈盒。之后，硬币电池放入一个由鳄鱼夹头电极线组成的自组装硬币电池盒中，并连接到一个电化学工作站 (CHI 6278E, CH Instrument, Inc.)。在 25 °C 下以 100 mA g⁻¹ 的电流密度进行充放电循环，在 0.01–3.0 V vs. Li^+/Li 范围内。在 TLS 01C2 的情况下，波长 ($\lambda = 0.6888 \text{ \AA}$) 和衍射强度通过与 CeO_2 粉末标准在 18 keV 的操作能量和 300 mA 的电子环电流下校准。在光束站结束时，Mar345 成像板区域探测器安装在二维 (2D) X 射线衍射模式下，以 60 s 的曝光时间收集衍射图案。GSAS-II 软件用于将收集的 2D 数据转换为一维衍射图案。

Electrochemical measurements

电极材料由 70 wt.% 活性材料、20 wt.% Super-P (Alfa Aesar, 99.5%) 作为导电碳和 10 wt.% 聚偏氟乙烯 (PVDF, Alfa Aesar) 作为粘合剂组成。在 N-甲基-2-吡咯烷酮 (NMP) 溶剂中均匀混合后，糊状物被涂在铜箔上，然后在 120 °C 下干燥 12 h。所得电极膜被制成直径为 12 mm 的圆形片，活性物质装载量约为 2.5 mg。正极片被装入 CR2032 型硬币电池中，在 Ar 填充的手套箱 (MBraun) 中进行电化学测量，其中金属锂箔作为对电极，玻璃纤维 (Whatman, Grade GF/B) 作为隔膜。电解质是 1 M LiPF_6 溶于乙腈 (EC) 和二甲基碳酸酯 (DMC) 中的体积比为 1:1。恒流充放电测试在 0.01–3.0 V vs. Li^+/Li 的范围内进行，使用 LAND 电池测试系统 (Jinnuo)。对应于 1 C 的电流密度为 500 mA g⁻¹。循环伏安 (CV) 曲线在三电极细胞中记录，Li 线作为参考和对电极，在 0.01 和 3.0 V 之间以 0.1 mV/s 的扫描速率扫描。在 RST5200 上进行电化学阻抗谱 (EIS) 测量，频率范围为 10 mHz – 100 kHz，AC 幅度为 5 mV，使用 Autolab 电化学工作站 (PGSTAT302N)。为了在充电/放电状态下进行原位 XRD 和 XPS 分析，选择硬币电池在充电/放电状态下拆解，工作电极用二甲基碳酸酯彻底清洗，以去除电解质，然后在 XRD 和 XPS 测量前对其进行处理。

Acknowledgements

This work was supported by the National Natural Science Foundation of China [grant number 21703147 and U1401248]; the Natural Science Foundations for the Young Scientist of Jiangsu Province [grant number BK20170338]; the General Financial Grant from the China Postdoctoral Science Foundation [grant number 2016M601876]. The Open Fund of Jiangsu Key Laboratory of Materials and Technology for Energy Conversion [grant number MTEC-2017M01]. The authors thank Testing and Analysis Center, Soochow University, Suzhou 215123, China. The authors also acknowledge Suzhou Key Laboratory for Advanced Carbon Materials and Wearable Energy Technologies, Suzhou 215006, China.

Conflict of Interest

The authors declare no conflict of interest.

Keywords: $\text{Bi}_2\text{Mo}_3\text{O}_{12}$ · binary metal oxide · lithium storage mechanism · MXene support · anode material

- [1] Y. Sun, N. Liu, Y. Cui, *Nat. Energy*. **2016**, *1*, 1–12.
- [2] X. Chen, Y. Zhu, B. Li, P. Hong, X. Luo, X. Zhong, L. Xing, W. Li, *Electrochim. Acta* **2017**, *224*, 251–259.
- [3] Y. Wu, R. Zeng, J. Nan, D. Shu, Y. Qiu, S.-L. Chou, *Adv. Energy Mater.* **2017**, *7*, 1700278.
- [4] Y. Chen, J. Li, G. Yue, X. Luo, *Nano-Micro Lett.* **2017**, *9*, 32.
- [5] F. Zheng, C. Yang, X. Xiong, J. Xiong, R. Hu, Y. Chen, M. Liu, *Angew. Chem. Int. Ed.* **2015**, *54*, 13058–13062; *Angew. Chem.* **2015**, *127*, 13250–13254.
- [6] F. Zheng, C. Yang, X. Ji, D. Hu, Y. Chen, M. Liu, *J. Power Sources* **2015**, *288*, 337–344.
- [7] F. Mueller, D. Bresser, V. S. K. Chakravadhanula, S. Passerini, *J. Power Sources* **2015**, *299*, 398–402.
- [8] R. Verrelli, J. Hassoun, *J. Power Sources* **2015**, *299*, 611–616.
- [9] M. Chen, D. Chen, Y. Liao, X. Zhong, W. Li, Y. Zhang, *ACS Appl. Mater. Interfaces* **2016**, *8*, 4575–4584.
- [10] X. Chen, Y. Zhang, H. Lin, P. Xia, X. Cai, X. Li, X. Li, W. Li, *J. Power Sources* **2016**, *312*, 137–145.
- [11] P. Lian, X. Zhu, S. Liang, Z. Li, W. Yang, H. Wang, *Electrochim. Acta* **2010**, *55*, 3909–3914.
- [12] C.-H. Yim, E. A. Baranova, F. M. Courtel, Y. Abu-Lebdeh, I. J. Davidson, *J. Power Sources* **2011**, *196*, 9731–9736.
- [13] Q. Q. Xiong, J. P. Tu, Y. Lu, J. Chen, Y. X. Yu, Y. Q. Qiao, X. L. Wang, C. D. Gu, *J. Phys. Chem. C* **2012**, *116*, 6495–6502.
- [14] D. Li, L.-X. Ding, S. Wang, D. Cai, H. Wang, *J. Mater. Chem. A* **2014**, *2*, 5625–5630.
- [15] J. Tang, S. Wu, T. Wang, H. Gong, H. Zhang, S. M. Alshehri, T. Ahamad, H. Zhou, Y. Yamauchi, *ACS Appl. Mater. Interfaces* **2016**, *8*, 2796–2804.
- [16] J. Zhang, A. Yu, *Sci. Bull.* **2015**, *60*, 823–838.
- [17] X. Hu, W. Zhang, X. Liu, Y. Mei, Y. Huang, *Chem. Soc. Rev.* **2015**, *44*, 2376–2404.
- [18] X. Zhao, J. Sui, F. Li, H. Fang, H. Wang, J. Li, W. Cai, G. Cao, *Nanoscale* **2016**, *8*, 17902–17910.
- [19] C. Wang, L. Wu, H. Wang, W. Zuo, Y. Li, J. Liu, *Adv. Funct. Mater.* **2015**, *25*, 3524–3533.
- [20] H. Zhang, L. Gao, Y. Gong, *Electrochim. Commun.* **2015**, *52*, 67–70.
- [21] D. Yuan, W. Yang, J. Ni, L. Gao, *Electrochim. Acta* **2015**, *163*, 57–63.
- [22] G. Wang, J. Ni, H. Wang, L. Gao, *J. Mater. Chem. A* **2013**, *1*, 4112–4118.
- [23] H. Li, P. Liu, N. Zhou, X. Huang, H. Wang, *Ceram. Int.* **2017**, *43*, 11967–11972.
- [24] R. Dai, Y. Wang, P. Da, H. Wu, M. Xu, G. Zheng, *Nanoscale* **2014**, *6*, 13236–13241.
- [25] Y. Li, M. A. Trujillo, E. Fu, B. Patterson, L. Fei, Y. Xu, S. Deng, S. Smirnov, H. Luo, *J. Mater. Chem. A* **2013**, *1*, 12123–12127.
- [26] Z. Deng, T. Liu, T. Chen, J. Jiang, W. Yang, J. Guo, J. Zhao, H. Wang, L. Gao, *ACS Appl. Mater. Interfaces* **2017**, *9*, 12469–12477.
- [27] H. Yin, M.-L. Cao, X.-X. Yu, H. Zhao, Y. Shen, C. Li, M.-Q. Zhu, *Mater. Chem. Front.* **2017**, *1*, 1615–1621.
- [28] C.-M. Park, S. Yoon, S.-I. Lee, H.-J. Sohn, *J. Power Sources* **2009**, *186*, 206–210.
- [29] T. Liu, Y. Zhao, L. Gao, J. Ni, *Sci. Rep.* **2015**, *5*, 9307.
- [30] C. Liang, M. Gao, H. Pan, Y. Liu, M. Yan, *J. Alloys Compd.* **2013**, *575*, 246–256.
- [31] J. R. Rodriguez, C. Belman-Rodriguez, S. A. Aguilera, Y. Zhang, H. Liu, V. G. Pol, *Chem. Commun. (Camb.)* **2018**, *54*, 11483–11486.
- [32] Y. Zheng, T. Zhou, X. Zhao, W. K. Pang, H. Gao, S. Li, Z. Zhou, H. Liu, Z. Guo, *Adv. Mater.* **2017**, *29*, 1700396.
- [33] J. Li, S. Xiong, Y. Liu, Z. Ju, Y. Qian, *ACS Appl. Mater. Interfaces* **2013**, *5*, 981–988.
- [34] Y. Zhang, C. Liu, X. Gao, Z. Luo, J. Hu, G. Zou, H. Hou, Z. Xu, X. Ji, *Nano Energy* **2020**, *68*, 104333.
- [35] H. B. Wu, J. S. Chen, H. H. Hng, X. W. Lou, *Nanoscale* **2012**, *4*, 2526–2542.
- [36] E. Luévanó-Hipólito, A. Martínez-de la Cruz, Q. L. Yu, H. J. H. Brouwers, *Appl. Catal. A* **2013**, *468*, 322–326.
- [37] A. Martínez-de la Cruz, S. Obregón Alfaro, *Solid State Sci.* **2009**, *11*, 829–835.
- [38] A. K. Kulkarni, M. S. Tamboli, D. Y. Nadargi, Y. A. Sethi, S. S. Suryavanshi, A. V. Ghule, B. B. Kale, *J. Solid State Chem.* **2020**, *281*, 121043.
- [39] S. Cao, C. Chen, T. Liu, Y. Tsang, X. Zhang, W. Yu, W. Chen, *Chem. Eng. J.* **2014**, *257*, 309–316.
- [40] A. V. Ghule, K. A. Ghule, S.-H. Tzing, J.-Y. Chang, H. Chang, Y.-C. Ling, *Chem. Phys. Lett.* **2004**, *383*, 208–213.
- [41] K. Ma, H. Jiang, Y. Hu, C. Li, *Adv. Funct. Mater.* **2018**, *28*, 1804306.
- [42] H.-J. Zhang, J. Shu, K.-X. Wang, X.-T. Chen, Y.-M. Jiang, X. Wei, J.-S. Chen, *J. Mater. Chem. A* **2014**, *2*, 80–86.
- [43] B. Guo, X. Fang, B. Li, Y. Shi, C. Ouyang, Y.-S. Hu, Z. Wang, G. D. Stucky, L. Chen, *Chem. Mater.* **2012**, *24*, 457–463.
- [44] W. Fang, N. Q. Zhang, L. S. Fan, K. N. Sun, *J. Power Sources* **2016**, *333*, 30–36.
- [45] M. Naguib, M. Kurtoglu, V. Presser, J. Lu, J. Niu, M. Heon, L. Hultman, Y. Gogotsi, M. W. Barsoum, *Adv. Mater.* **2011**, *23*, 4248–4253.
- [46] B. Anasori, M. R. Lukatskaya, Y. Gogotsi, *Nat. Rev. Mater.* **2017**, *2*, 16098.
- [47] J. Halim, S. Kota, M. R. Lukatskaya, M. Naguib, M.-Q. Zhao, E. J. Moon, J. Pitcock, J. Nanda, S. J. May, Y. Gogotsi, M. W. Barsoum, *Adv. Funct. Mater.* **2016**, *26*, 3118–3127.
- [48] M. Naguib, J. Halim, J. Lu, K. M. Cook, L. Hultman, Y. Gogotsi, M. W. Barsoum, *J. Am. Chem. Soc.* **2013**, *135*, 15966–15969.
- [49] T. Hu, M. Hu, Z. Li, H. Zhang, C. Zhang, J. Wang, X. Wang, *Phys. Chem. Chem. Phys.* **2016**, *18*, 20256–20260.
- [50] M. Alhabeb, K. Maleski, B. Anasori, P. Lelyukh, L. Clark, S. Sin, Y. Gogotsi, *Chem. Mater.* **2017**, *29*, 7633–7644.
- [51] X. Li, X. Yin, M. Han, C. Song, H. Xu, Z. Hou, L. Zhang, L. Cheng, *J. Mater. Chem. C* **2017**, *5*, 4068–4074.
- [52] C. Yang, Y. Liu, X. Sun, Y. Zhang, L. Hou, Q. Zhang, C. Yuan, *Electrochim. Acta* **2018**, *271*, 165–172.
- [53] R. Gruar, C. J. Tighe, L. M. Reilly, G. Sankar, J. A. Darr, *Solid State Sci.* **2010**, *12*, 1683–1686.

Manuscript received: May 14, 2020
 Revised manuscript received: July 20, 2020
 Accepted manuscript online: July 27, 2020
 Version of record online: August 19, 2020